H^+ ion-implantation energy dependence of electronic transport properties in the MeV range in *n*-type silicon wafers using frequency-domain photocarrier radiometry

Chinhua Wang[a)]
Institute of Modern Optical Technologies, Suzhou University, Suzhou, Jiangsu 215006, People's Republic of China

Andreas Mandelis and Jordan Tolev
Center for Advanced Diffusion-Wave Technologies, Department of Mechanical and Industrial Engineering, University of Toronto, Toronto, Ontario M5S 3G8, Canada

Bernd Burchard and Jan Meijer
Rubion, Ruhr-Universitaet Bochum, D-44780 Bochum, Germany

(Received 26 February 2007; accepted 8 May 2007; published online 27 June 2007)

Industrial *n*-type Si wafers (resistivity of 5–10 Ω cm) were H^+ ion implanted with energies between 0.75 and 2.00 MeV, and the electronic transport properties of the implanted layer (recombination lifetime, carrier diffusion coefficient, and front-surface and implanted-interface recombination velocities s_1 and s_2) were studied using photocarrier radiometry (PCR). A quantitative fitting procedure to the diffusing photoexcited free-carrier density wave was introduced using a relatively simple two-layer PCR model *in lieu* of the more realistic but substantially more complicated three-layer model. The experimental trends in the transport properties of H^+-implanted Si layers extracted from the PCR amplitude and phase data as functions of implantation energy corroborate a physical model of the implanted layer in which (a) overlayer damage due to the light H^+ ions decreases with increased depth of implantation at higher energies, (b) the implanted region damage close to the interface is largely decoupled from the overlayer crystallinity, and (c) the concentration of implanted H^+ ions decreases at higher implantation energies at the interface, thus decreasing the degree of implantation damage at the interface proper. © *2007 American Institute of Physics*. [DOI: 10.1063/1.2748868]

I. INTRODUCTION

H^+ implantation of semiconductors and proton irradiation on semiconductor wafers have grown to become important tools in improving the performance of semiconductor devices by modifying or tailoring the electronic parameters such as the minority carrier lifetime. Accurate control and evaluation of the electronic properties of the implanted semiconductor samples have been an important topic in H^+ implantation or irradiation. Proton implantation is in use for many types of industrial applications:[1–4] lifetime adjustment in high power devices by producing, e.g., oxygen vacancy (OV) defects (the so-called *A* centers) is not only a major focus but also the influence of defect centers on the carrier mobility, numbers, etc., is an important issue.[5] Proton implantation is also used in the production of memory or logic devices.[6,7] Furthermore, another type of hydrogen induced donor function has been successfully applied in industrial production of, e.g., modern superjunction devices.[8] This is a very important topic for proton implantation from the industrial point of view because it allows changing the doping profile of a power device down to considerable depth. However, from the fundamental point of view, questions such as does hydrogen produce stable hydrogen vacancy (HV) centers or how does a hydrogen associated donor shallow thermal donors (STD) (H) act still remain unanswered. The stabilities of the defect centers and their interactions with the doping atom, trapping centers, or metals are additional problems.[9] Much attention has been paid to the effect of proton and other light ion irradiation on the carrier lifetime of substrates and devices.[10–12] The conventional method of measuring the carrier lifetime under high-injection conditions is the open circuit voltage decay (OCVD),[13] which is a contacting method. Frequency-domain photocarrier radiometry (PCR),[14] a dynamic modulated photoluminescence technique, was recently introduced and found to be a sensitive method for characterization, depth profiling, and subsurface defect imaging of semiconductor materials. In contrast to photomodulated thermoreflectance (PMR) (Ref. 15) and to photothermal radiometry (PTR),[16] PCR is a purely radiative optoelectronic diffusive carrier-wave detection methodology, which is sensitive to the electrical transport parameters of semiconductor materials and is free of nonradiative (thermal) contributions to the signal. There have been several theoretical and experimental studies for the PCR response of ion-implanted semiconductors.[17,18] One of the most important features of ion-implanted samples is the inhomogeneous damage of the crystalline structure along the depth direction resulting from the interaction of the implanted ions and the semiconductor substrate. The implanted ions traverse the sample surface and eventually reside at a certain depth de-

[a)]Electronic mail: chinhua.wang@suda.edu.cn

pending on their energy, which forms an inhomogeneous subsurface structure. However, defects are mainly generated close to the end of the traveling ion range, especially at moderate doses. The thickness of the implanted inhomogeneous layer could be in the range from submicrometer to tens of micrometers, depending on the energy of the implantation and the size of the ions. To address properties of the implanted layer and the substrate, layered structure models have been developed and employed for experimental interpretations.[19,20] Recently, Li *et al.*[21] developed a three-layer theoretical model which provides a good explanation of PCR signal dependence with implanted ion dose. This model, however, encounters a practical challenge in quantitative evaluation of the implanted wafers, in which the electronic parameters are obtained via a multiparameter fitting process. In a three-layer model, the uppermost (surface) layer and the second layer are assumed to be the region traversed by the implanted ions and the region where ions eventually reside, respectively. The substrate (third) layer is assumed to remain intact. Attempts to measure electronic parameters for the first and the second layer through multiparameter fits to photothermal or photocarrier radiometric frequency response data result in very complicated or impractical fitting procedures due to the fact that too many parameters (such as optical absorption coefficient, lifetime, and carrier diffusion coefficient for each layer, as well as recombination velocities at the front and back surfaces and at the interface) are involved in the fitting process. To reduce the number of fitted parameters encountered using a three-layer model, Li *et al.*[22] explored the possibility of establishing an equivalence between a three-layer and a single-layer structure. Due to the relatively very thin (submicrometer) top and implanted layers formed under implantation with conventional ions used for microelectronic device fabrication (B^+, P^+, As^+), the effect of the implanted layer on the overall PCR signal can be modeled as an effective surface layer without significant compromise in terms of accuracy and validity. When the implantation depth substantially increases, however, the single-layer equivalence of the three-layer model is challenged. In this work, we demonstrate a quantitative fitting process using a two-layer model to reduce the number of fitting parameters encountered in the three-layer model for H^+ implantation and enhance the validity and the accuracy, which are compromised in the single-layer model. The uppermost (surface) layer and the second layer in the three-layer model are merged to an effective single layer based on the fact that the second layer is usually very thin ($\sim 2\ \mu$m) when compared with the upper layer with a thickness of tens of micrometers, typical of implantation energy ranges of several hundred keV up to the MeV level. By incorporating an interface recombination velocity, the effective impact on the PCR signal of the thin second (damaged) layer with high implanted ion concentration is taken into account. The developed theoretical algorithm was further used to evaluate H^+ implanted Si wafers with various implantation energies. The best-fitted effective electronic parameters of the implanted layer are in good correlation with the implantation energy, which provides a reasonable balance between complexity and accuracy, thus demonstrating the excellent predictive ability of PCR regarding electronic transport properties and other optoelectronic phenomena associated with high energy ion-implantation processes.

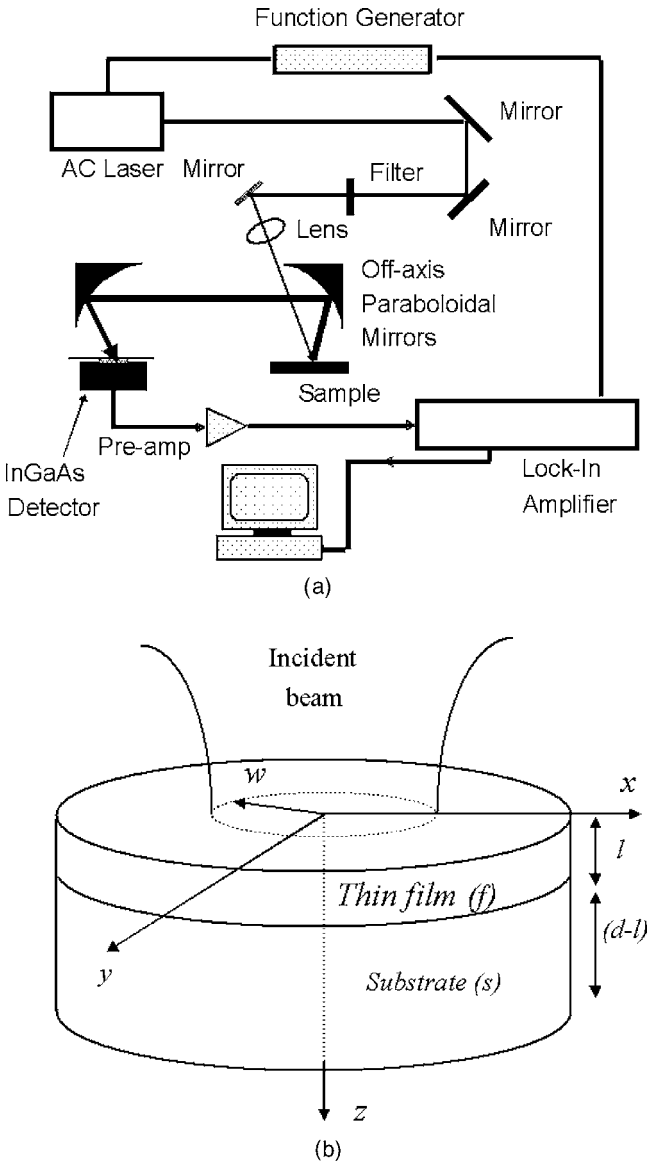

FIG. 1. PCR measurement setup (a) and configuration of a two-layer ion-implanted system (b).

II. TWO-LAYER THEORETICAL MODEL

The conventional PCR setup for semiconductor studies is shown in Fig. 1(a). Details are given in Sec. IV and can also be gleaned in Refs. 21 and 22. The sample geometry and incident laser beam configuration for PCR detection are shown in Fig. 1(b). The exciting laser beam is assumed to be of finite size with a Gaussian profile, $\exp(-r^2/w^2)$, where w is the laser beam spot size. Its intensity is modulated at angular frequency $\omega(=2\pi f)$ and the beam is focused on an (effectively) two-layer semiconductor surface. The radius of the semiconductor wafer is assumed to be very large compared to the radius of the laser beam and to the detector aperture. The direction of the incident beam is normal to the surface of the sample. Any azimuthal variations of the PCR signal are ignored; i.e., the semiconductor is considered to be

isotropic thermally, optically, and electronically within one carrier or thermal diffusion length, whichever is larger, from the zero coordinate at the center point of the optical excitation. The thickness of the two-layer sample is d and l the thickness of the top layer (thin film).

When a semiconductor is illuminated with super-band-gap light of photon energy $h\nu$, electrons in the valence band absorb the incident energy and are excited across the band gap E_g to the conduction band, leaving an equal number of holes in the valence band. The excess electrons and holes attain thermal equilibrium with the lattice through phonon interactions on a very short time scale, releasing the excess energy $h\nu - E_g$ in the form of heat. In an indirect-gap semiconductor such as Si, the photogenerated excess electrons and holes diffuse for a short time (known as carrier lifetime τ) before they recombine through nonradiative processes, releasing thermal energy to the lattice. In PCR measurements the thermal midinfrared (Planck mediated) emissions are filtered out and only near-infrared (NIR) radiative emissions from the free-carrier wave are detected by an appropriate NIR detector and spectrally matched filter combination. The optically injected three-dimensional excess carrier densities N_i ($i=f,s$ stands for *thin film* and *substrate*, respectively) in the two-layer system are calculated from the following carrier transport equations:

$$\nabla^2 N_i(r,z,\omega) - {\sigma_{ni}}^2 N_i(r,z,\omega) = -\frac{G_i(r,z,\omega)}{D_{ni}}, \quad i=f,s, \tag{1a}$$

where D_{ni} is the carrier diffusivity of the thin film and the substrate and

$$\sigma_{ni} = \sqrt{\frac{1+i\omega\tau_i}{D_{ni}\tau_i}}, \tag{1b}$$

$$G_f(r,z,\omega) = \frac{\alpha_f \eta_{nf} P_0(1-R)}{h\nu\pi w^2} \exp\left(-\frac{r^2}{w^2} - \alpha_f z\right), \tag{1c}$$

$$G_s(r,z,\omega) = \frac{\alpha_s \eta_{ns} P_0(1-R)\exp(-\alpha_f l)}{h\nu\pi w^2} \times \exp\left[-\frac{r^2}{w^2} - \alpha_s(z-l)\right]. \tag{1d}$$

Here P_0 and $h\nu$ are the power and the photon energy of the incident radiation, respectively, R is the surface reflectivity of the sample, α_i ($i=f,s$) is the optical absorption coefficient of thin film and substrate, respectively, and η_{ni} ($i=f,s$) is the optical-to-electronic conversion quantum efficiency. The boundary conditions for the carrier density wave at the interfaces $z=0$, l, and d are

$$D_{nf}\frac{\partial N_f(r,0,\omega)}{\partial z} = s_1 N_f(r,0,\omega), \tag{2a}$$

$$D_{nf}\frac{\partial N_f(r,l,\omega)}{\partial z} - D_{ns}\frac{\partial N_s(r,l,\omega)}{\partial z} = -s_2 N_f(r,l,\omega), \tag{2b}$$

$$N_f(r,l,\omega) = N_s(r,l,\omega), \tag{2c}$$

$$D_{ns}\frac{\partial N_s(r,d,\omega)}{\partial z} = -s_3 N_s(r,d,\omega), \tag{2d}$$

where s_1, s_2, and s_3 are the recombination velocities at the front surface ($z=0$), the interface ($z=l$), and the rear ($z=d$) surface, respectively. Taking advantage of the cylindrical symmetry of the boundary-value problem, we can use the Hankel transformation method. By taking the Hankel transforms of Eqs. (1) and (2), we can obtain solutions for the free-carrier densities in Hankel space, namely, $\tilde{N}_i(\lambda,z,\omega) \times (i=r,s)$, which are the transforms of the desired solutions $N_i(r,z,\omega)$ in conventional cylindrical coordinates. The Hankel transforms of the carrier-wave components of the PCR signal from the thin film and the substrate, $\tilde{F}_i(\lambda,\omega)$, are obtained from $\tilde{N}_i(\lambda,z,\omega)$ by integrating over the thickness of the thin film and the substrate, respectively,[19] which takes into account deep-lying volume Planck-radiation emission from photogenerated and diffused carriers, according to Kirchhoff's law of detailed balance,[14]

$$\tilde{F}_f(\lambda,\omega) = \int_0^l \tilde{N}_f(\lambda,z,\omega)dz, \tag{3}$$

$$\tilde{F}_s(\lambda,\omega) = \int_l^d \tilde{N}_s(\lambda,z,\omega)dz, \tag{4}$$

where

$$\tilde{N}_f(\lambda,z,\omega) = C_1\exp(b_{nf}z) + C_2\exp(-b_{nf}z) + C_3\exp(-\alpha_f z), \tag{5}$$

$$\tilde{N}_s(\lambda,z,\omega) = C_4\exp(b_{ns}z) + C_5\exp(-b_{ns}z) + C_6\exp(-\alpha_s z). \tag{6}$$

Constants C_3 and C_6 are determined from the particular solutions of Eq. (1) corresponding to the thin film and the substrate, respectively. $C_i(i=1,2,4,5)$ can be determined from the boundary conditions, Eq. (2), in Hankel space. Full expressions for these parameters are given in the Appendix. The collection efficiency of the NIR detector can be taken into account by integrating the resulting expression over the effective aperture of the detector, assuming it to be a disk of radius a,

$$\tilde{S}_{\mathrm{PCR},i}(\lambda,\omega) = \frac{1}{\pi a^2}\int_0^a \tilde{F}_i(\lambda,\omega)J_0(\lambda\rho)\rho d\rho, \quad i=f,s. \tag{7}$$

Here $J_0(x)$ is the Bessel function of the first kind of order zero. Finally, inverting the Hankel transform $\tilde{S}_{\mathrm{PCR},i}(\lambda,\omega)$ yields

$$S_{\mathrm{PCR},i}(\omega) = \frac{1}{\pi a}\int_0^\infty \tilde{F}_i(\lambda,\omega)J_1(\lambda a)d\lambda, \quad i=f,s, \tag{8}$$

where $J_1(x)$ is the Bessel function of the first kind of order one. In Eqs. (5) and (6) the definition ${b_{ni}}^2 = \lambda^2 + {\sigma_{ni}}^2$ ($i=f,s$) was made. The overall PCR signal can be expressed as a summation of the contributions from thin film and substrate,

$$S_{\mathrm{PCR}}(\omega) = \frac{1}{\pi a}\int_0^{\infty} [\tilde{F}_f(\lambda,\omega) + \tilde{F}_s(\lambda,\omega)]J_1(\lambda a)d\lambda. \qquad (9)$$

Equation (9) represents the frequency-dependent PCR signal detected by the IR detector and will be directly compared with, and fitted to, the experimental data.

III. SIMULATIONS

To show the difference between the two-layer and the one-layer behavior as a function of modulation frequency, we first demonstrate a result of multiparameter best fits to an implanted three-layer structure using a one-layer and a two-layer theoretical model. To determine the electronic transport properties of ion-implanted wafers via a multiparameter fit to a single-layer or a two-layer model, we created a set of PCR data arrays which include 32 amplitude and 32 phase points in the modulation frequency range from 0.1 to 1000 kHz with the three-layer model.[21] Then we performed multiparameter fits of the simulated data to the single-layer or two-layer model via a least-squares process to extract the effective transport properties of the ion-implanted Si wafers. In the one-layer fitting process, the three-layer structure is characterized with an equivalent single (monolithic) layer, in which the equivalent carrier transport properties (recombination lifetime τ, carrier diffusion coefficient D, and front- and back-surface recombination velocities s_1 and s_2) are extracted from the best-fit algorithm. In the two-layer fitting process, the three-layer structure is characterized via an equivalent model, in which the structure is divided into two layers: The first layer is the implanted region which comprises the thickness traversed by the implant ions and the layer in which the ions eventually reside. The second layer lies beneath the first layer and can be considered to remain intact after implantation (i.e., the structure is not damaged during the implantation process). In the fitting process, the equivalent transport parameters of the surface layer and the interface between the surface and second layers, are extracted. Since ion implantation modifies mainly the optical and electronic transport processes in the implanted layer and it is known that the modification of the optical absorption coefficient in the implanted layer does not affect the overall PCR signal phase and the normalized amplitude (i.e., the shape of the amplitude curve),[22] we discuss only the effect of the electronic transport properties of the implanted layer on the fitted effective parameters of the ion-implanted wafers. In the multiparameter fitting process, the following variance between the theory and the experiment is minimized:

$$\text{variance} = \sum_{i=1}^{2} \frac{\sum_{j=1}^{N} [P_{i,\mathrm{fit}}(f_j) - P_{i,3L}(f_j)]^2}{\sum_j [P_{i,3L}(f_j)]^2},$$

where $i=1,2$ represent the amplitude and the phase, respectively. N is the total number of data points (32 points in this case). $P_{i,3L}$ is the amplitude or phase simulated with the three-layer model and $P_{i,\mathrm{fit}}$ is the fitted PCR amplitude or phase calculated with the single-layer and the two-layer model. The fitting error is defined as the square root of the square variance in percent (%). During the fitting procedure, three transport properties, τ, D, and s_1, were set as free parameters in the single-layer model. All four transport properties of the implanted layer and the interface, τ_1, D_1, s_1, and s_2, were set free parameters in the two-layer model. Here s_2, is the interface velocity. In both fitting procedures, self-normalized amplitudes were used, in which the PCR amplitude at the lowest frequency point simulated with the three-layer model and those calculated with the single-layer model or the two-layer model were both normalized to unity prior to fitting, thus simplifying the fitting procedure.

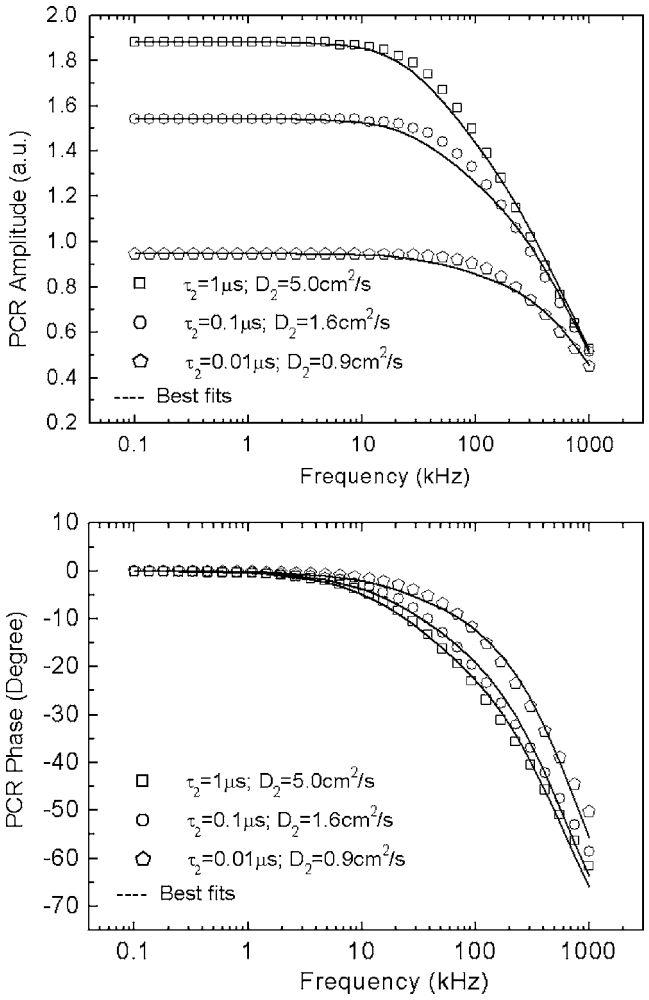

FIG. 2. Fitting results using, one-layer equivalence.

Figures 2 and 3 show the fitted PCR amplitude and phase as a function of the modulation frequency using the single-layer and the two-layer model, respectively. The curves consisting of discrete symbols are calculated using the three-layer model with the same parameters for an ion-implanted semiconductor wafer at various levels of electronic damage caused by ion implantation, before the onset of optical damage. These curves serve as "experimental" data. In the calculation, the parameters of the three-layer system and the geometry used are shown in Fig. 4. The value of 6.6×10^4 m^{-1} of the absorption coefficient of c-Si used for the implanted layers in these fits is reasonable because as implantation dose increases, electronic damage occurs before the onset of optical damage.[23,24] The back surface recombi-

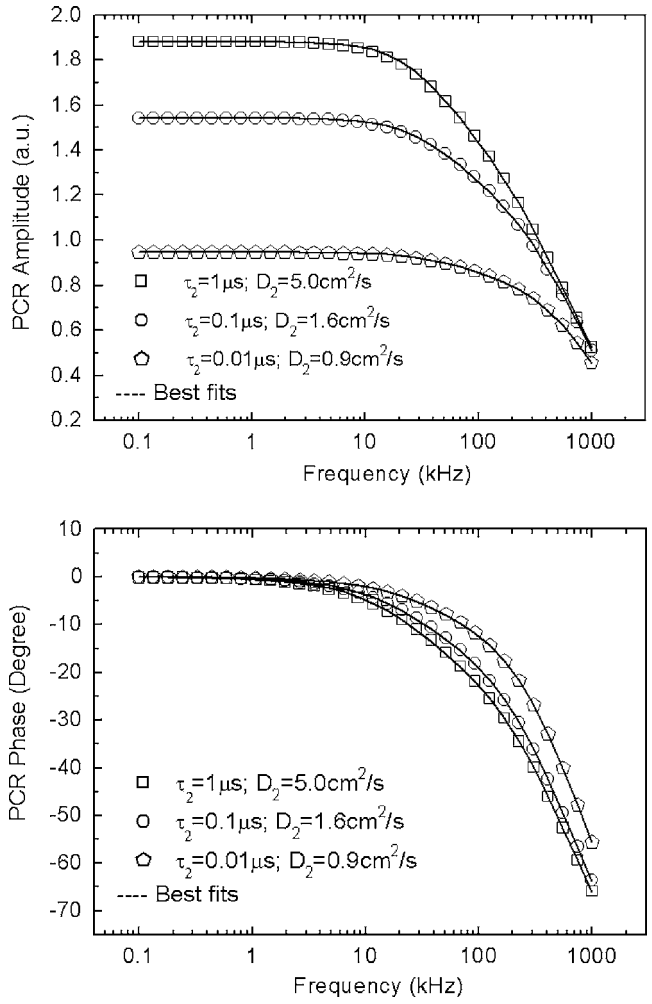

FIG. 3. Fitting results using two-layer equivalence.

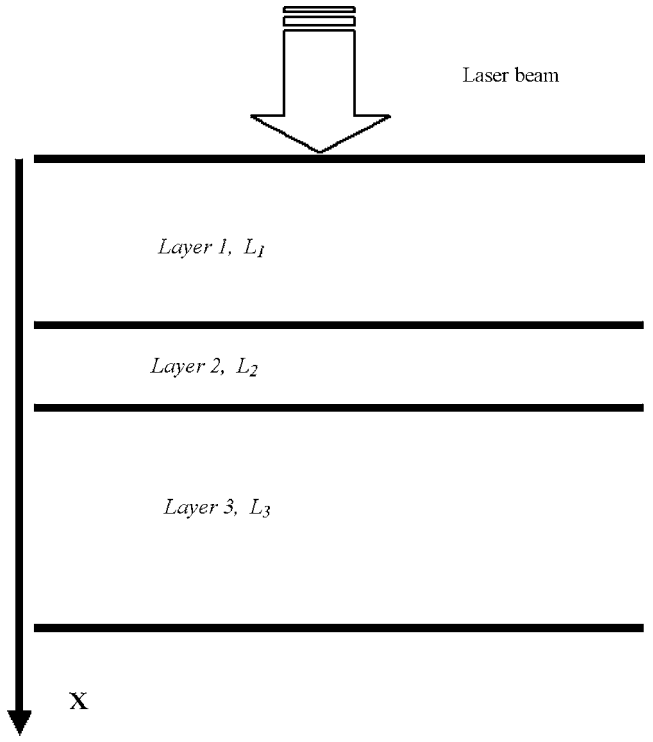

FIG. 4. Cross section of the three-layer geometry. Surface layer: the carrier lifetime (τ_1), the diffusion coefficient (D_1), and the thickness (L_1) of the surface layer are assumed to be 0.5 μs, 3.5 cm^2/s, and 20 μm, respectively. Second layer: τ_2 and D_2 vary representing different levels of electronic damage, the thickness L_2 is assumed to be 3 μm. Third (undamaged) substrate layer: τ_3, D_3, and L_3 are assumed to be 20 μs, 35 cm^2/s, and 482 μm, respectively. Total thickness of the wafer is 505 μm. The optical absorption coefficients ($\alpha_1, \alpha_2, \alpha_3$) of the three layers are assumed to be the same: 6.6×10^4 m^{-1}, i.e., the absorption coefficient of crystalline silicon (c-Si) at 830 nm wavelength.

nation velocity s_3 is assumed to be 10^5 cm/s because simulations show that the PCR signal is not very sensitive to s_3 in a wide range of values from 1×10^3 to 10^6 cm/s. The radius of the pump laser beam was taken to be 25 μm and the effective size of the detector was assumed to be 55 μm. Different levels of electronic damage in the second layer are characterized by the carrier lifetime (τ_2) and diffusion coefficient (D_2) of the layer. Three different levels of damage in terms are assumed in the calculation resulting in the following combinations of (τ_2, D_2): 1 μs, 5 cm^2/s, 0.1 μs, 1.6 cm^2/s, and 0.01 μs, 0.9 cm^2/s.

The simulated PCR amplitude and phase using the foregoing data were subsequently fitted with the single-layer and two-layer models, and the results are shown in Figs. 2 and 3, respectively (solid lines). The detailed fitting parameters are listed in Tables I and II. Comparison between Figs. 2 and 3 shows significantly better fits using the two-layer model than those using the single-layer model. The fitting error using the two-layer model is typically one order of magnitude lower than that of the single-layer model, as shown in Tables I and II. Using the single layer model, it is found that it is difficult to fit the entire frequency-scan curve to the simulated three-layer model. This means the equivalence between a three-layer and a single layer structure is much compromised. The deviation between the simulated three-layer and the fitted single-layer suggests that a more accurate fitting model must be used than the single-layer model.

It should be noted that the equivalence between the single- and three-layer models may be acceptable when the implanted layer (i.e., the second layer in a three-layer sequence) is very thin (<0.5 μm) and very close to the surface (~10 nm), which is true for a H^+ implantation energy of ~50 keV. In this case, the full effect of the implanted layer can be attributed to front-surface damage when the typical thickness of a wafer is $\sim500-600$ μm, while the bulk lifetime and the diffusion coefficient remain essentially the same as that of the undamaged substrate.[22] However, when the implantation energy increases, the ions penetrate much deeper than those of lower energies (e.g., ~20 μm when H^+ implantation energy reaches ~1 MeV), and the width of the region where the ions eventually reside is about $2-3$ μm, which is also assumed in the present three-layer calculation. In this case, the effect of the surface and second layers on the PCR signal is shown not to be equivalent to surface photocarrier recombination phenomena only. From Table I it is seen that all fitted values of the single-layer lifetime, electronic diffusion coefficient, and front-surface recombination velocity change with increasing electronic damage, which implies that the effects of changes in the bulk of the implanted layer on the PCR signal must be considered when the

TABLE I. Fitted results for simulated data with various electronic damage rates using one-layer equivalence.

Fitting conditions	Input (τ_2, D_2) (μs and cm^2/s)	Fitted lifetime (τ) (μs)	Fitted D (cm^2/s)	Fitted s_1 (cm/s)	Fitting error (%)
Self-normalized amplitude used in the fitting, S_2 fixed at 1×10^5 cm/s	1.0: 5.0	7.97	20.97	9238.7	4.48
	0.1: 1.6	4.18	24.09	10 703.8	6.44
	0.01: 0.9	1.36	25.22	3 0762.8	9.21

implantation depth increases. This is in contrast to the case of very shallow implantation, in which only the front-surface recombination velocity changes while the bulk parameters such as lifetime and electronic diffusivity remain essentially unaltered.[22]

Table II shows the results using the two-layer equivalent model with multiparameter best-fit curves shown in Fig. 3. By introducing the interface recombination velocity s_2, contributions of the implanted (second) layer to the three-layer model can be mainly attributed to interface recombination phenomena. Compared with the single-layer model in which the effect of the very thin implanted layer is averaged over the entire thickness and is incorporated in the bulk and surface parameters (τ_1, D_1, and s_1) almost uniformly, the effect of the implanted layer in the two-layer model is averaged within the top layer only ($\sim$23 μm in this case). Although four parameters are introduced in the fitting process, it is seen that the electronic damage in the implanted layer is very sensitive to the interface recombination velocity s_2, which is in agreement with the nature of the thin implanted layer embedded in the wafer. The fitted s_2 values change much more sensitively than s_1 in the single layer model for the same range of the electronic damage and the fitting error is well below 1%, showing a much better equivalence between three-layer and two-layer models than that between three-layer and single-layer models. Based on these conclusions, in the following section we will use the two-layer model to characterize H^+ implanted Si wafers and compare the results with that of single layer model.

It is instructive to discuss the fitted parameters from the single- and two-layer models. In the single-layer model, three parameters (τ_1, D_1, and s_1) are employed as fitting parameters, whereas in the two-layer model four parameters are fitted. In both cases the fitted parameters are the "effective" values corresponding to the layer represented by those parameters. The fitted parameters may be very different from the actual values, especially in the single-layer model, where any changes of electronic and optical properties in the relatively thin ($\sim$20 μm) ion-implantation-damaged layer are represented by property values averaged over the entire layer ($\sim$500 μm), including the undamaged substrate. In the two-layer model, the ion-implantation damage is represented by the top effective layer only ($\sim$23 μm), whereas the substrate (482 μm) remains unaffected. Therefore, the parameters extracted from the two-layer model are expected to be much closer to the "real" values in each layer, a reasonable expectation which also results in a much better fit to the data curves than that from the single-layer model.

IV. MATERIALS, EXPERIMENTAL RESULTS, AND DISCUSSION

A series of proton implanted n-Si wafers was prepared and measured. These samples were H^+ implanted with various energies (ranging from 0.75 to 1.5 MeV) with a dose of 3×10^{14} cm^{-2}. Detailed information of the fixed-dose sample matrix is shown in Fig. 5 with the corresponding implantation energy and the ion depth. The depth of implantation area was calculated using the program SRIM (Ref. 25) and is shown above the first row on the table of Fig. 5. The dots shown in Fig. 5 are associated with numerical labels of the samples under measurement. A typical depth profile of the ion-implanted silicon is shown in Fig. 6 for 1.5 MeV implantation energy, depicting the ion concentration along the depth direction. The center of the peak ion concentration (i.e., implantation depth) is around 30.8 μm with a full width at half maximum (FWHM) of 2 μm. Based on the fact that the FWHM of the ion peak is $\sim$7% of the surface layer (30 μm) and $\sim$0.4% of the total thickness (505 μm), the ion concentration peak can be considered as the interface. As a result of the very narrow FWHM in Fig. 6, the implanted silicon can be roughly divided into two layers with an interface boundary at the ion peak. The top layer represents the region traversed by the H^+ ions. The second layer represents the intact

TABLE II. Fitted results for simulated data with various electronic damage rates using two-layer equivalence.

Fitting conditions	Input (τ_2, D_2) (μs and cm^2/s)	Fitted lifetime (τ_1) (μs)	Fitted D_1 (cm^2/s)	Fitted s_1 (cm/s)	Fitted s_2 (cm/s)	Fitting error (%)
Self-normalized amplitude used in the fitting, S_3 fixed at 1×10^5 cm/s	1: 5.0	3.92	5.42	4256.9	1798.2	0.69
	0.1: 1.6	1.91	4.48	4189.5	4632.4	0.72
	0.01: 0.9	1.58	4.43	4107.1	26 877.4	0.59

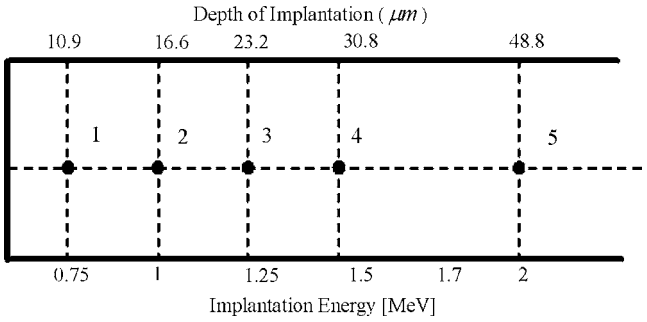

FIG. 5. Implantation energy matrix of H^+ implanted silicon wafers at fixed dose of 3×10^{14} cm^{-2}.

substrate, while the peak represents the depth where the ions eventually reside. In comparison to the two-layer model, where four parameters, i.e., lifetime, electronic diffusivity, optical absorption coefficient, and thickness of the ion layer are involved, the two layer system considered here characterizes the implanted wafer with the parameters of the first layer combined with the effect at the interface of the ion peak in the form of a boundary condition.

Experiments with the series of H^+ implanted wafers described in Fig. 5 were performed to correlate the electronic transport parameters to the implantation energies at the given dose. The PCR experimental setup is shown in Fig. 1(a). Briefly, a tunable Ti:sapphire laser pumped by a 10 W 532 nm laser was used as the excitation source. The laser was operated at 830 nm wavelength and the laser power was 23 mW. The laser beam spot size was measured to be approximately $w=402$ μm. The near-IR emission from the sample was collected and focused through a pair of reflective objectives onto an InGaAs detector, preamplifier, and optical cut-on filter assembly. The effective radius of the detector was estimated to be 500 μm. The spectral response range of the detector was 0.8–1.8 μm. The optical filter further served to block any leakage of the excitation source into the active element of the detector.

For each silicon wafer, the PCR signal was recorded as a function of modulation frequency with a lock-in amplifier (LIA). The frequency scan was performed from

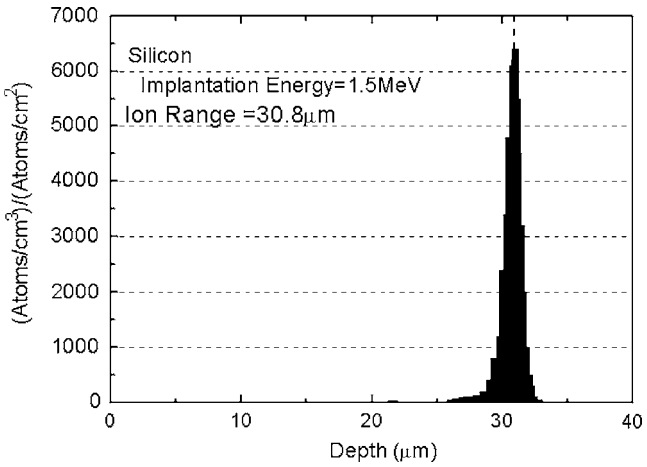

FIG. 6. Typical ion depth profile of H^+ implanted silicon at 1.5 MeV implantation energy.

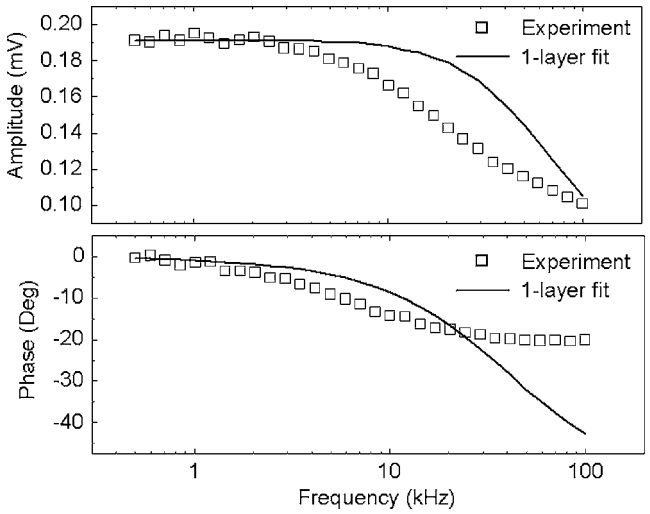

FIG. 7. Experimental data and the corresponding fits using the single layer for sample 1 with implantation energy of 0.75 MeV.

0.5–100 kHz with a total of 31 points, logarithmically equispaced. To eliminate the influence of instrumental transfer function, the amplitude and phase of the PCR signal were normalized by the detector signal recorded with the scattered light of the excitation beam (in this case the filter in front of the detector was removed so that a very small fraction of the scattered modulated incident light would be detected without driving the detector to saturation).

The wafers were first characterized using the single-layer model. Figure 7 shows a typical fitting result for sample 1, which has the lowest implantation energy. It is seen that the best fits between the experimental data and the single-layer theoretical result are not acceptable. The fitting error is as high as 53%, which implies that there is no equivalence between the experimental data and the single-layer model. Subsequently, the experimental data were fitted using the two-layer model. In the two-layer fitting process, a high quality nonimplanted silicon wafer from the same batch as the implanted wafer was measured first to determine transport parameters which served as those of the substrate (undamaged) layer in the simplified two-layer system. The fitted lifetime and the diffusion coefficient were 17.0 μs and 17.5 cm^2/s, respectively. The optical absorption coefficient of 6.6×10^4 m^{-1} for *c*-silicon wafer at 830 nm was used for the undamaged second layer. These substrate parameters were used for all the wafers from the same batch. The corresponding thicknesses of the implanted layer for all wafers (i.e., the top layer) are shown in Fig. 5. In the fitting process, a proportionality factor C, which represents the ratio of the theoretical value and the voltage output of the experimental system, was first determined using reference sample 1. The constant C was then fixed for the rest of the samples. This is reasonable because the experimental conversion factor between PCR radiation received by the detector and signal voltage output remained unchanged during all measurements. Therefore, the *relative* PCR amplitudes among all the samples reflect meaningful *changes* in optical and electronic properties of the wafers after implantation. The fixed value of C also reduces by one the set of fitting parameters and

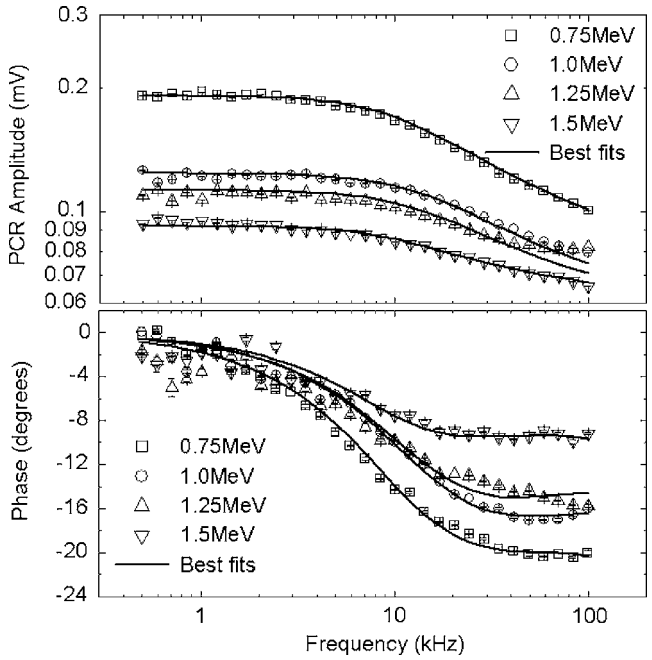

FIG. 8. Experimental frequency dependence of PCR amplitudes and phases and the corresponding best fits for several H^+ implantation energies. The implantation dose was 3×10^{14} cm^{-2}.

helps enhance the accuracy and uniqueness of the fit for a series of samples with relative transport property changes. In our measurements the value of C was found to be 43.09 MKS units.

Figure 8 shows the experimental amplitudes and phases and the corresponding best-fitted theoretical curves from H^+-implanted wafers at various energies. It is seen that the experimental data were all fitted reasonably well (error less than 10%) using the two-layer model. The amplitude of the PCR signal decreases with implantation energy, as expected, due to the thicker implantation layers and increased electronic defect densities which impede radiative recombination, enhancing the nonradiative recombination pathway, instead. The phase lag also decreases sensitively with increasing implantation energy, in contrast to the dose dependence of the PCR signal in which the phase shows a slow change with dose.[22] This occurs because increased energy implies a deeper damaged layer with decreased participation of the free-carrier wave in the undamaged substrate toward the determination of the mean carrier-wave density centroid which thus moves closer to the surface (decreased phase lag with increasing energy). On the other hand, substrate free-carrier-wave participation does not greatly diminish when the implantation energy (depth) remains fixed and dose varies because implantation dose change does not sensitively affect the effective thickness of the implanted layer, so the PCR phase remains essentially unchanged.

The extracted parameters from the best fits of Fig. 8 are shown in Fig. 9. Downwards from the top in Fig. 9, the fitted parameters are lifetime (τ_1), diffusion coefficient (D_1), optical absorption coefficient (α_1), front-surface recombination velocity (s_1), and interface recombination velocity (s_2), respectively. It is seen that, except in the case of 0.75 MeV implantation, the lifetime (τ_1) and the front recombination

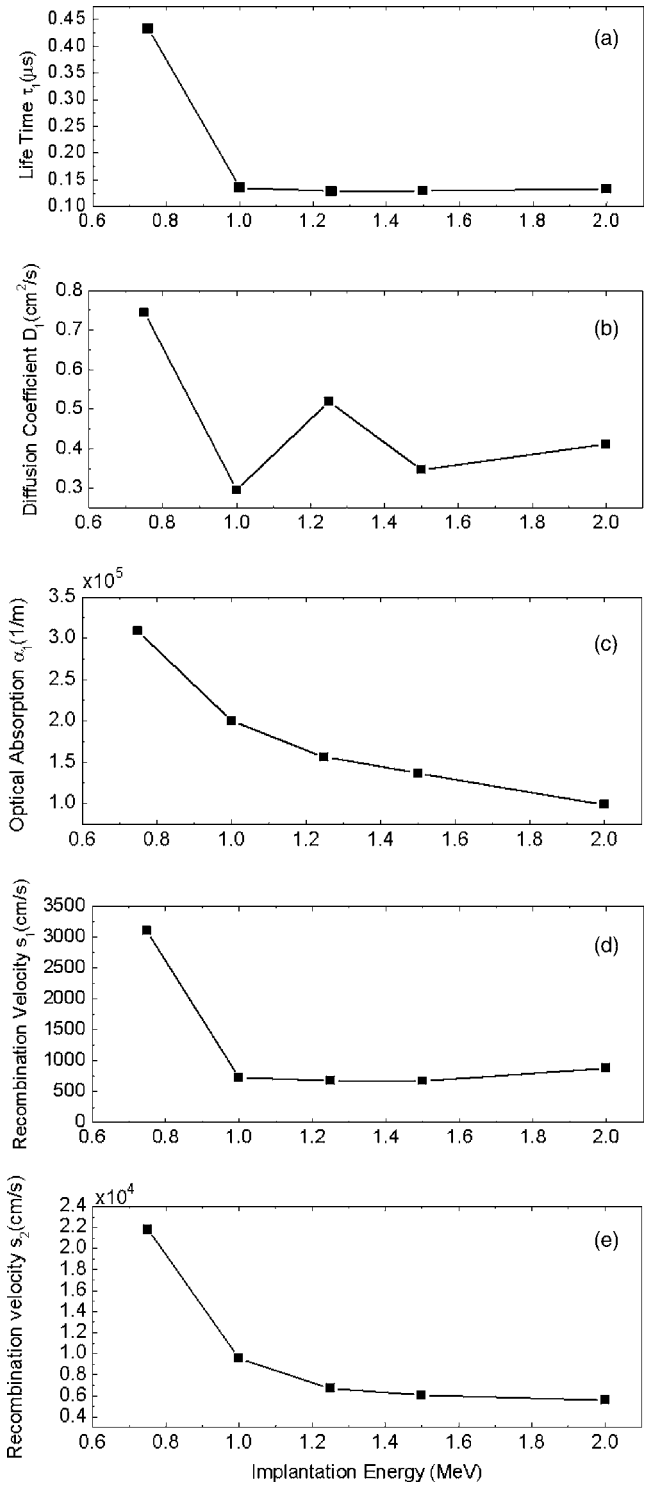

FIG. 9. Extracted parameters from the best fits of experimental data shown in Fig. 8.

velocity s_1 saturate for energies higher than 1 MeV, which is consistent with the simulation results in Table II, in which s_1 and τ_1 are not sensitive to the assumed electronic damage in layer 2 under deep implantation. The diffusion coefficient shows a nonmonotonic behavior with implantation energy probably due to experimental or fitting tolerance error. Note that the diffusion coefficient range in Fig. 9 is fairly narrow and the measured values could be construed to be constant within experimental or fitting error. Further computational

tests demonstrated that the variations in D_1 within the range shown in Fig. 9(b) do not significantly change the remaining best-fit results, further supporting the hypothesis that fluctuations in D_1 at, or above, 1 MeV may be due to statistical error in the data affecting the best fit to an essentially constant D_1 value. It is interesting to note that all parametric curves in Fig. 9 show constancy or diminished sensitivity at energy values at or above 1 MeV, preceded by much steeper slopes between 0.75 and 1 MeV. Figure 9(c) shows that the optical absorption coefficient of the implanted layer decreases monotonically with energy, and Fig. 9(d) shows that the front-surface recombination velocity rapidly saturates above 1 MeV. Similarly, the interface recombination velocity s_2 decreases in a more gradual manner reminiscent of the optical absorption coefficient. These trends can be qualitatively understood by the fact that higher energies result in increasingly more remote locations for the actual damaged region (the narrow implanted interface in Fig. 6), which thus leaves the overlying crystal structure [especially the uppermost of ~ 5 μm ($=1/\alpha_1$ at 830 nm for *c*-Si)]relatively less damaged by the light H^+ ion at increasingly larger depths and thus characterized by a decreased optical absorption coefficient. The surface recombination velocity s_1 shows a steep decrease above 0.75 MeV and remains either constant or shows a slight increase above 1.5 MeV, perhaps due to optical annealing of the residual surface damage. This behavior is also consistent with noninteracting deep implanted layer and crystalline surface, as expected since it is well established that most of the defects are generated close to the deep end of implantation range. The behavior of the interface velocity s_2 can be understood by additional data (not shown here), showing that H^+-ion depth profiles exhibit decreasing peak concentrations and thus increased crystalline integrity with increasing energy. In summary, the experimental trends in the transport properties of H^+-implanted Si layers extracted from the PCR amplitude and phase data as functions of implantation energy yield valuable information about the evolution of electronic and optical integrity of the implanted layer and its two interfaces nondestructively. They corroborate a physical model in which the increased penetration depth of the light proton implants with energy leaves the front surface with lower optoelectronic defect densities and the back interface with lower peak implant concentrations also amounting to lower defect densities acting as recombination centers. The less defective near-surface region further exhibits lower absorption coefficient and higher recombination lifetime.

V. CONCLUSIONS

Industrial *n*-type Si wafers (resistivity of 5–10 Ω cm) were H^+ ion implanted and their electronic transport properties were studied using photocarrier radiometry. A quantitative fitting procedure was introduced using a relatively simple two-layer PCR model *in lieu* of the more realistic but substantially more complicated three-layer model. It was found that the two-layer model provides an optimal tool for characterizing H^+ ion implants, balancing accuracy, complexity, and validity as compared to the simpler, but inaccurate, one-layer model. For shallow depth implantation (low energy, ~tens of keV), the equivalence between the three-layer model and the single-layer model may be acceptable since in this case, the ion-implantation depth can be considered as a surface effect. However, when the implantation energy increases, the deviation between the three-layer and single-layer models increases significantly, and the equivalence between the two is no longer valid for light, deep penetrating ions such as H^+ when the energy and depth increase to MeV levels and tens of micrometers, respectively. Based on the two-layer fitting algorithm, a matrix of H^+ implanted *n*-type Si wafers with fixed dose and different energies was characterized. It was found that while the lifetime, diffusion coefficient, and front-surface recombination velocity essentially saturate at or above 1 MeV, the optical absorption coefficient of the surface layer and the interface recombination velocity decreases monotonically with energy. These results suggest that (a) overlayer damage due to the light H^+ ions decreases with increased depth of implantation at higher energies, (b) the implanted region damage close to the substrate interface is largely decoupled from the overlayer crystallinity, and (c) the concentration of implanted H^+ ions decreases at higher implantation energies at the interface, most likely due to ion scattering at nonzero directions within the overlayer, thus decreasing the degree of implantation damage at the interface proper. Furthermore, it is noted that the absolute values of the recombination lifetime measured with PCR are about ten times smaller than those of the OV center measured by OVCD.[26] This is reasonable, as the present samples were measured in their as-implanted state, whereas the OVCD measurements were performed with annealed specimens.

ACKNOWLEDGMENTS

One of the authors (A.M.) is grateful to the Alexander von Humboldt Foundation for a Research Award at Ruhr University Bochum which made this research possible. The support of the Natural Sciences and Engineering Research Council of Canada (NSERC) through a Discovery Grant to AM is also gratefully acknowledged. The support of the Educational Committee of Jiangsu Province (Contract No. Q2108608) and of an initializing research fund of Suzhou University to one of the authors (C.-H.W.) is gratefully acknowledged.

APPENDIX

Complex quantities used in Eqs. (5) and (6) are given as follows:

$$C_3 = -\frac{\alpha_f \eta_f P_0 (1-R)}{D_{nf} h\nu\pi(\alpha_f^2 - b_{nf}^2)} e^{-\lambda^2 w^2/4}, \tag{A1}$$

$$C_6 = -\frac{\alpha_s \eta_s P_0 (1-R)\exp(-\alpha_f l)}{D_{ns} h\nu\pi(\alpha_s^2 - b_{ns}^2)} e^{-\lambda^2 w^2/4},$$

$$C_4 = C_4^* e^{-b_{ns} l}, \tag{A2}$$

with

$$C_4^* = \frac{C_3[\xi_3 e^{-\alpha_f l} - \Delta_1(1+\Gamma_2)e^{-b_{nf}l}] + C_6[\xi_2\Delta_3 e^{(\alpha_s - b_{ns})(l-d)} - \xi_4]}{\xi_2\Gamma_3 - \xi_1 e^{2b_{ns}(l-d)}} e^{2b_{ns}(l-d)},$$

$$C_5 = C_5^* e^{b_{ns}l}, \tag{A3}$$

with

$$C_5^* = \frac{C_3\Gamma_3[\xi_3 e^{-\alpha_f l} - \Delta_1(1+\Gamma_2)e^{-b_{nf}l}] + C_6[\xi_1\Delta_3 e^{(\alpha_s + b_{ns})(l-d)} - \xi_4\Gamma_3]}{\xi_2\Gamma_3 - \xi_1 e^{2b_{ns}(l-d)}},$$

$$C_1 = C_1^* e^{-b_{nf}l}, \tag{A4}$$

with

$$C_1^* = \frac{C_4^*(1+\Phi_1) + C_5^*(1-\Phi_1) - C_3(1-\Delta_2)e^{-\alpha_f l} + C_6(1-\Sigma_1)}{(1+\Gamma_2)},$$

$$C_2 = C_2^* e^{b_{nf}l}, \tag{A5}$$

with

$$C_2^* = \frac{-C_4^*(\Phi_1 - \Gamma_2) + C_5^*(\Phi_1 + \Gamma_2) - C_3(\Gamma_2 + \Delta_2)e^{-\alpha_f l} + C_6(\Gamma_2 + \Sigma_1)}{(1+\Gamma_2)}, \tag{A6}$$

where

$$\Gamma_1 = \frac{D_{nf}b_{nf} - s_1}{D_{nf}b_{nf} + s_1}, \tag{A7}$$

$$\Gamma_2 = \frac{D_{nf}b_{nf} + s_2}{D_{nf}b_{nf} - s_2}, \tag{A8}$$

$$\Gamma_3 = \frac{D_{ns}b_n + s_3}{D_{ns}b_{ns} - s_3}, \tag{A9}$$

$$\Delta_1 = \frac{D_{nf}\alpha_f + s_1}{D_{nf}b_{nf} + s_1}, \tag{A10}$$

$$\Delta_2 = \frac{D_{nf}\alpha_f - s_2}{D_{nf}b_{nf} - s_2}, \tag{A11}$$

$$\Delta_3 = \frac{D_{ns}\alpha_s - s_3}{D_{ns}b_{ns} - s_3}, \tag{A12}$$

$$\Phi_1 = \frac{D_{ns}b_{ns}}{D_{nf}b_{nf} - s_2}, \tag{A13}$$

$$\Sigma_1 = \frac{D_{ns}\alpha_s}{D_{nf}b_{nf} - s_2}, \tag{A14}$$

$$\xi_1 = (\Phi_1 - \Gamma_2) + \Gamma_1(1+\Phi_1)e^{-2b_{nf}l}, \tag{A15}$$

$$\xi_2 = (\Phi_1 + \Gamma_2) - \Gamma_1(1-\Phi_1)e^{-2b_{nf}l}, \tag{A16}$$

$$\xi_3 = (\Delta_2 + \Gamma_2) - \Gamma_1(1-\Delta_2)e^{-2b_{nf}l}, \tag{A17}$$

$$\xi_4 = (\Sigma_1 + \Gamma_2) - \Gamma_1(1-\Sigma_1)e^{-2b_{nf}l}. \tag{A18}$$

[1] J. Meijer, B. Burchard, K. Ivanova, B. E. Volland, I. W. Rangelow, M. Rub, and G. Deboy, J. Vac. Sci. Technol. B **22**, 152 (2004).
[2] M. Bakowski, N. Galster, A. Hallen, and A. Weber, ABB Semiconductors AG, ISPSD, Weimar (1997).
[3] P. Leveque, A. Hallen, B. G. Svensson, J. Wong-Leung, C. Jagadish, and V. Privitera, Eur. Phys. J.: Appl. Phys. **23**, 5 (2003).
[4] K. Yokota, S. Nakase, K. Nakamura, F. Miyashita, M. Tannjou, S. Sakai, and H. Takano, Eur. Phys. J.: Appl. Phys. **27**, 129 (2004).
[5] S. Hayama, G. Davies, and K. M. Itoh, J. Appl. Phys. **96**, 1754 (2004).
[6] P. Cova, R. Menozzi, and M. Portesine, 23rd International Conference on Microelectronics, 2002, Vol. 1, pp. 143–146.
[7] B. Sopori, Y. Zhang, and N. M. Ravindra, J. Electron. Mater. **30**, 1616 (2001).
[8] D. H. Macdonald, H. Maeckel, S. Doshi, W. Brendle, A. Cuevas, J. S. Williams, and M. J. Conway, Appl. Phys. Lett. **82**, 2987 (2003).
[9] R. Siemieniec, F.-J. Niedernostheide, H.-J. Schulze, W. Suedkamp, U. Kellner-Werdehausen, and J. Lutz, J. Electrochem. Soc. **153**, G108 (2006).
[10] R. Siemieniec, W. Sudkamp, and J. Lutz, Solid-State Electron. **46**, 891 (2002).
[11] D. K. Schroder, *Semiconductor Material and Device Characterization* (Wiley, New York, 1990).
[12] A. Hauser, M. Spiegel, P. Fath, and E. Bucher, 28th IEEE Photovoltaic Specialists Conference, Vol. 1, pp. 323–326 (IEEE, New York, 2000).
[13] D. K. Schroder, *Semiconductor Material and Device Characterization* (Wiley, New York, 1990).
[14] A. Mandelis, J. Batista, and D. Shaughnessy, Phys. Rev. B **67**, 205208 (2003).
[15] W. L. Smith, A. Rosencwaig, and D. L. Willenborg, Appl. Phys. Lett. **47**, 584 (1985).
[16] A. Salnick, A. Mandelis, F. Funak, and C. Jean, J. Appl. Phys. **71**, 1531 (1997).
[17] A. Mandelis, J. Appl. Phys. **97**, 083508 (2005).
[18] J. Batista, A. Mandelis, and D. Shaughnessy, Appl. Phys. Lett. **82**, 4077 (2003).
[19] M. Nestoros, Y. Karmiotis, and C. Christofides, J. Appl. Phys. **82**, 6220 (1997).

[20]A. Salnick and J. Opsal, Rev. Sci. Instrum. **74**, 545 (2003).
[21]B. Li, D. Shaughnessy, A. Mandelis, J. Batista, and J. Garcia, J. Appl. Phys. **95**, 7832 (2004).
[22]B. Li, D. Shaughnessy, A. Mandelis, J. Batista, and J. Garcia, J. Appl. Phys. **96**, 186 (2004).
[23]Ch. Wilbertz, K. L. Bhatia, W. Kraetschmer, and S. Kalbitzer, Mater. Sci. Eng., B **2**, 325 (1989).
[24]A. Salnick and J. Opsal, J. Appl. Phys. **91**, 2874 (2002).
[25]J. F. Ziegel and J. P. Biersack, SRIM, www.srim.org.
[26]R. Siemieniec, D. Schipanski, W. Südkamp, and J. Lutz, Proceedings of the 8th European Conference on Power Electronics and Applications (EPE'99), Lausanne, 1999, p. 99.